JACS
JOURNAL OF THE AMERICAN CHEMICAL SOCIETY
Article
Cite This: J. Am. Chem. Soc. XXXX, XXX, XXX−XXX
pubs.acs.org/JACS

Synergistic Boron Doping of Semiconductor and Dielectric Layers for High-Performance Metal Oxide Transistors: Interplay of Experiment and Theory

Xinan Zhang,[†,‡,⊥] Binghao Wang,[†,⊥] Wei Huang,[†] Yao Chen,[†] Gang Wang,[†] Li Zeng,[∥] Weigang Zhu,[†] Michael J. Bedzyk,[∥] Weifeng Zhang,[*,‡] Julia E. Medvedeva,[*,§] Antonio Facchetti,[*,†] and Tobin J. Marks[*,†,∥]

[†]Department of Chemistry and the Materials Research Center, Northwestern University, 2145 Sheridan Road, Evanston, Illinois 60208, United States

[‡]School of Physics and Electronics, Key Laboratory of Photovoltaic Materials, Henan University, Kaifeng, 475004, PR China

[§]Department of Physics, Missouri University of Science and Technology, Rolla, Missouri 65409, United States

[∥]Applied Physics Program, Department of Materials Science and Engineering, and the Materials Research Center, Northwestern University, 2220 Campus Drive, Evanston, Illinois 60208, United States

Supporting Information

ABSTRACT: We report the results of a study to enhance metal oxide (MO) thin-film transistor (TFT) performance by doping *both* the semiconductor (In_2O_3) and gate dielectric (Al_2O_3) layers with boron (yielding IBO and ABO, respectively) and provide the first quantitative analysis of how B doping affects charge transport in these MO dielectric and semiconducting matrices. The impact of 1−9 atom % B doping on MO microstructure, morphology, oxygen defects, charge transport, and dielectric properties is analyzed together, in detail, by complementary experimental (microstructural, electrical) and theoretical (ab initio MD, DFT) methods. The results indicate that B doping frustrates In_2O_3 crystallization while suppressing defects responsible for electron trapping and carrier generation. In the adjacent Al_2O_3 dielectric, B doping increases the dielectric constant and refractive index while reducing leakage currents. Furthermore, optimized solution-processed TFTs combining IBO channels with 6 atom % B and ABO dielectrics with 10 atom % B exhibit field effect mobilities as high as 11 $cm^2\ V^{-1}\ s^{-1}$, current on/off ratios $>10^5$, threshold voltages = 0.6 V, and superior bias stress durability.

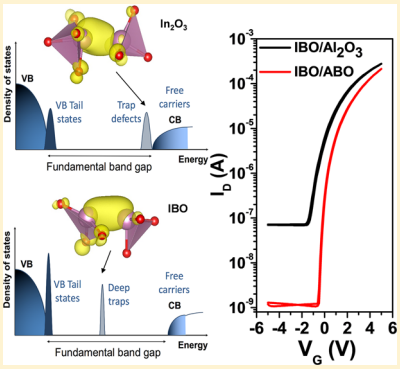

INRODUCTION

Amorphous metal oxides (a-MOs) have received increasing attention owing to their substantial carrier mobilities, low processing temperatures, environmental stability, good visible region optical transparency, and electrical/morphological uniformity over large areas.[1] Indeed, a-MO properties can complement or exceed those of silicon thin-film transistors (TFTs) for multiple applications, including high-definition flat panel and OLED displays. Commercial a-MO films are typically grown by capital-intensive physical or chemical vapor deposition techniques such as RF magnetron sputtering or atomic layer deposition, and are then patterned using expensive subtractive multistep photolithographic processes.[2,3] However, solution-based methods for thin-film fabrication are gaining acceptance because of their simplicity, low cost, easy control of chemical stoichiometry, and scalability.[4,5] Furthermore, independent of the TFT semiconductor growth and processing methodology, a compatible, high-quality gate dielectric must be employed to ensure reliability, operational stability, and mimimum power dissipation.

Indium oxide (In_2O_3) is among the most heavily investigated MOs, having a band gap larger than 3.1 eV, high intrinsic carrier concentration ($N = 10^{17}-10^{21}\ cm^{-3}$), and large electron field effect mobility ($\mu \approx 10-50\ cm^2\ V^{-1}\ s^{-1}$), thereby offering an effective MO host matrix for several classes of high-performance MO-based TFTs.[6,7] Nevertheless, undoped In_2O_3 films are often polycrystalline and the oxygen vacancies governing the carrier concentration are challenging to control, frequently affording In_2O_3 TFTs with less than optimal current modulation (low I_{on}/I_{off} ratios), poor bias stress stability, unacceptable threshold voltages, and poor uniformity.[7,8] Thus, In_2O_3 TFT performance reported by several groups using the same TFT architecture/dielectric (SiO_2) and growth conditions can differ significantly, with μ varying >10x![9−11]

Doping with metal cations (X = Ga^{3+}, Zn^{2+}, Si^{4+}, Hf^{4+}) to yield ternary or quaternary oxides of formula IXO or IXZO (Z

Received: June 18, 2018
Published: September 5, 2018

DOI: 10.1021/jacs.8b06395
J. Am. Chem. Soc. XXXX, XXX, XXX−XXX

= Zn) is a conventional strategy for In_2O_3 amorphization,[12−15] Such transition and post-transition metal ions with large spherically symmetrical *n*s-orbitals ($n \geq 4$) provide a dispersive conduction band for electron transport, even in the amorphous state. From Shanmugam's theory,[16] Lewis acid strength ($L = z/r^2$, where z = the atomic core charge number and r = the ionic radius) and dopant metal-oxide bond dissociation energy (E_{M-O}) are key parameters that stabilize MOs against O vacancy formation. Among known and potential dopants, note that boron has a very large B−O bond dissociation energy (808.8 kJ mol^{-1}; Table S1, Supporting Information)[16−18] that would likely suppress O vacancies in In_2O_3 TFTs. Furthermore, B has large L and z/r^2 values,[16] which should polarize the electron cloud away from O anions, and also reduce carrier scattering. Together these possibilities suggest that B dopants may enhance MO TFT performance by functioning as carrier suppressors. In possible confirmation of this strategy, Parthiban and Kwon RF sputtered 22 atom % B-doped In−Zn−O TFTs to achieve $\mu \sim 10$ $cm^2/(V\ s)$,[18] while Stewart et al. sputtered 18 atom % B-doped In_2O_3 and reported $\mu \sim 4$ $cm^2/(V\ s)$.[19] Also, solution-phase B-doping was reported for ZnO TFTs to achieve $\mu \sim 1.2$ $cm^2/(V\ s)$ at 8 atom % B.[14]

In the same vein, realizing solution-processed a-MO TFT gate dielectrics rivaling or surpassing incumbent, CVD-grown Si_3N_4 in performance remains a challenge. Critical properties such as high dielectric constant for low-voltage operation, dense film formation for low gate leakage currents and high breakdown voltage, and minimal interface state densities for stable operation must be achieved.[20] Electrons trapped in the gate insulator are responsible for severe bias stress degradation in IGZO TFTs,[21] and O vacancies originating from ionic bonding in high-*k* oxides may cause charge-trap mobility degradation and enhanced parasistic leakage currents. To our knowledge, the only example of B-doping a TFT gate dielectric is the work of Baik et al. in which an 8 atom % doped peroxo-zironium oxide dielectric enabled In_2O_3 mobilities as high as 39 $cm^2/(V\ s)$.[11] The mechanism was suggested to involve greater densification of the dielectric film and interfacial effects.

Here we report the use of boron as an efficient, simultaneous dopant for *both* semiconducting In_2O_3 (IBO) and high-*k* dielectric Al_2O_3 (ABO) films and demonstrate their integration in the first all-B-doped IBO/ABO TFTs. All MO films are fabricated by solution processing using low-temperature combustion synthesis,[22−24] which enables efficient and expedient screening of multiple B-doped In_2O_3 (IBO) and B-doped Al_2O_3 (ABO) film compositions. The impact and mechanism of 1−9 atom % B doping on the MO microstructure, morphology, oxygen defects, charge transport, and dielectric properties is analyzed together, in detail, with complementary experimental diffraction/scattering, electrical, and ab initio molecular dynamics (MD) liquid-quench simulations and density-functional theory (DFT) calculations. The combined results indicate that in In_2O_3 B-doping affects the oxygen defects associated with weak In−O bonding, making the unstable defects more localized and thus suppressing excess carrier concentrations and affording superior IBO switching characteristics. In contrast, for Al_2O_3 B-doping, the comparable Al−O and B−O bond strengths result in changes to the Al coordination number which bring about favorable changes in the ABO refractive index and dielectric properties. Thus, high-performance low-voltage oxide TFTs are demonstrated by combining optimal IBO with 6 atom % B/[In + B] and ABO with 10 atom % B/[Al+B] compositions as the semiconductor and dielectric layer, respectively, affording an optimized field effect mobility of 11.3 $cm^2\ V^{-1}\ s^{-1}$, a threshold voltage of 0.6 V, a current on/off ratio of 2×10^5, and a subthreshold swing of 0.17 V dec^{-1}, as well as excellent bias stress stability. These results provide a clear fundamental understanding of how boron affects the chemical environment and charge transport properties of MO matrices, opening the way for far broader utilization.

EXPERIMENTAL SECTION

Precursor Solutions. All precursor materials (99.999 mol % trace metals basis) were purchased from Sigma-Aldrich and used without further purification. Indium nitrate, $In(NO_3)_3{\cdot}xH_2O$ (0.05 M), and 0.05 M boric acid (H_3BO_3), or 0.1 M aluminum nitrate, $Al(NO_3)_3{\cdot}xH_2O$, were dissolved in 10 mL of 2-methoxyethanol. For the In_2O_3 and Al_2O_3 precursors, acetylacetone (AcAcH) in a molar ratio to metal of 2:1 and ammonium hydroxide (28% NH_3 in H_2O) with volumetric ratio to AcAcH of 1:2 were then successively added. The metal nitrates are the metal sources and oxidizers, and AcAcH is the fuel. After the In_2O_3 and Al_2O_3 precursor solutions were stirred for 3 h, measured amounts of boric acid were added to achieve the desired B/[In + B] content of 0, 3, 6, and 9 atom % boron and B/[Al + B] content of 0, 5, 10, and 15 atom % B in the solutions. The solutions were next stirred overnight at 25 °C and then filtered through a 0.2 μm PTFE membrane filter prior to spin coating.

Device Fabrication. Bottom-gate top-contact structures were used for the TFTs. A heavily doped Si wafer with a 300 nm thermally grown SiO_2 layer was used as the substrate. The heavily doped Si serves as the gate electrode, and the SiO_2 layer as the gate insulator. The substrate was ultrasonically cleaned with acetone and isopropyl alcohol, and then treated with an O_2 plasma for 5 min to eliminate organic contaminants and to improve the coating of the films. Then the IBO precursor solutions were spin-coated on the SiO_2 at 3500 rpm for 30 s in a dry air glovebox and subsequently annealed on a hot plate for 20 min at 300 °C. This process was repeated four times and the film thicknesses measured by X-ray reflectivity (XRR) were 8.5−8.9 nm. For characterizing the high-*k* dielectric devices, ABO solutions were directly spin-coated on heavily doped Si at 3000 rpm for 30 s, followed by annealing at 300 °C for 20 min. After repeating the above operation four times, the film was then postannealed at 450 °C for 1 h. Metal−insulator−semiconductor (MIS) structures were fabricated with 40 nm Al as top electrode by thermal evaporation. The area of electrode is 0.2 mm × 0.2 mm. For low-voltage TFT fabrication, the IBO films were spin-coated on the above optimized ABO dielectric. Next, 40 nm Al source/drain electrodes were deposited on the channel layer by thermal evaporation (Denton Vacuum Explorer) through a shadow mask to create a channel length of 100 μm, and channel width of 1000 μm.

Thin Film and Device Characterization. Grazing incidence X-ray diffraction (GIXRD) and XRR measurements used Cu Kα radiation (λ = 1.542 Å) from a Rigaku ATXG diffractometer with a multilayer mirror. The GIXRD measurements were performed at an incident angle of 0.5°. Films morphologies were measured with a Veeco Dimension Icon atomic force microscopy (AFM) system in the tapping mode. X-ray photoelectron spectroscopy (XPS) was performed on a Thermo Scientific Escalab 250 Xi spectrometer at a base pressure of 5×10^{-10} mbar (UHV). XPS spectra were collected after etching the film surface for about 3 nm to minimize surface contamination. Film refractive indices were measured using a J. A. Woollam M2000U ellipsometer and fit with a Cauchy model.

C−*V* measurements were conducted by applying a small alternating current signal of 50 mV amplitude and 10 kHz frequency while the DC voltage was swept from a negative to positive bias and back again. Current−voltage (*I*−*V*) characteristics were measured under ambient conditions using an Agilent B1500A semiconductor parameter analyzer. The threshold voltage (V_T) was extracted from the saturation region by plotting the drain current ($I_{DS}^{1/2}$) vs the gate

DOI: 10.1021/jacs.8b06395
J. Am. Chem. Soc. XXXX, XXX, XXX−XXX

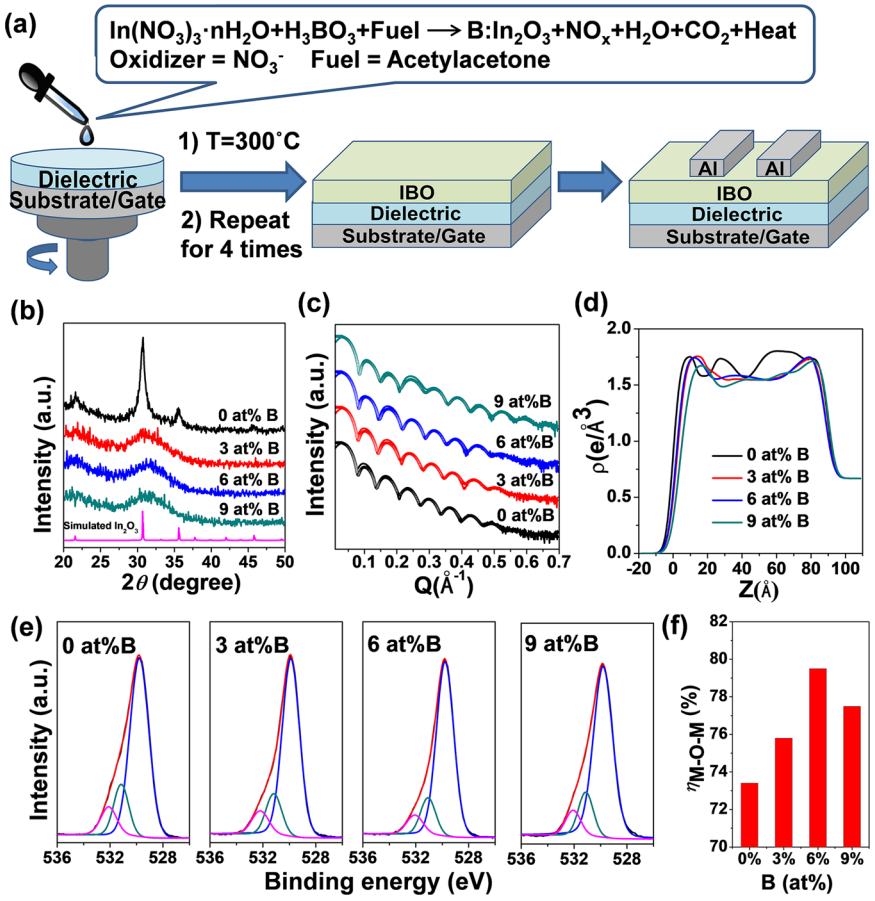

Figure 1. Characterization of IBO films. (a) Schematic of the IBO film and TFT fabrication process. (b) GIXRD patterns. (c) XRR patterns. (d) XRR determined electron density profiles with $Z = 0.0$ at the film surface. (e) Oxygen 1s XPS peaks with best-fit results. (f) η_{M-O-M} of IBO thin films with increasing B atom %.

voltage (V_{GS}) and extrapolating to an I_{DS} value of 0. The dielectric can be modeled as two capacitors in series, $1/C_i = 1/C_{diel} + 1/C_{SiO_2}$. The areal capacitance of the native oxide on the Si bottom electrode is 1382 nF cm^{-2} assuming a 2.5 nm thick SiO_2 layer with a dielectric constant of 3.9. The field-effect mobility (μ) and the subthreshold slope (SS) of the fabricated transistor were extracted using eqs 1 and 2. Here C_i is the capacitance per unit area of oxide insulator, V_T is the threshold voltage, and V_{GS} is the gate voltage. W and L are channel width and length, respectively.

$$I_{DS} = \left(\frac{\mu C_i W}{2L}\right)(V_{GS} - V_T)^2 \quad (1)$$

$$SS = \left(\frac{d(\log_{10} I_{DS})}{dV_{GS}}\right)^{-1} \quad (2)$$

Computational Methods. The amorphous metal oxide structures were generated using first-principles molecular dynamics as implemented in the Vienna Ab Initio Simulation Package (VASP).[25−28] These calculations are based on the DFT with Perdew−Burke−Ernzerhof (PBE) functional[29] within the projector augmented-wave method.[30,31] The local structural characteristics in amorphous oxide materials can be made based on the average pair correlation function (eq 3)[32] where l_i and l_{min} are individual metal−oxygen bond lengths and minimum bond length in the polyhedron, respectively. Using

$$l_{av} = \frac{\sum_i l_i \exp(1 - (l_i/l_{min})^6)}{\sum_i \exp(1 - (l_i/l_{min})^6)} \quad (3)$$

The pair correlation function, the effective coordination number N_{ECN} can be calculated for each polyhedron according to eq 4.[33] The atomic configurations obtained from the ab initio MD simulations were optimized using the PBE functional.

$$N_{ECN} = \sum_i \exp(1 - (l_i/l_{av})^6) \quad (4)$$

For the optimization, a cutoff energy of 500 eV and the 4 × 4 × 4 Γ-centered k-point mesh was used; the atomic positions were relaxed until the Hellmann−Feynman force on each atom was below 0.01 eV/Å. Next, the electronic and optical properties of amorphous In_2O_3- and Al_2O_3-based structures were calculated using the hybrid Heyd−Scuseria−Ernzerhof (HSE06) approach[34,35] with a mixing parameter of 0.25 and a screening parameter μ of 0.2 Å^{-1}. Refractive index was derived from the frequency-dependent dielectric function calculated within independent particle approximation as implemented in VASP. The imaginary part is related to the optical absorption at a given frequency, and is determined based on the electronic transitions of the hybrid functional solution. The real part of the complex dielectric function is obtained using Kramers−Kronig relations. To analyze the localized states in the band gap and near the band edges, the inverse participation ratio (IPR) of an orbital $\Psi_n(\vec{r}_i)$ can be found from ab initio density-functional calculations according to eq 5,[17]

$$IPR(\Psi_n) = N\frac{\sum_{i=1}^{N} |\Psi_n(\vec{r}_i)|^4}{\left|\sum_{i=1}^{N} |\Psi_n(\vec{r}_i)|^2\right|^2} \quad (5)$$

where N is the number of volume elements in the cell and i is the index of the volume element. The structural properties and charge density distribution in the amorphous oxides were analyzed and plotted using VESTA.[36]

DOI: 10.1021/jacs.8b06395
J. Am. Chem. Soc. XXXX, XXX, XXX−XXX

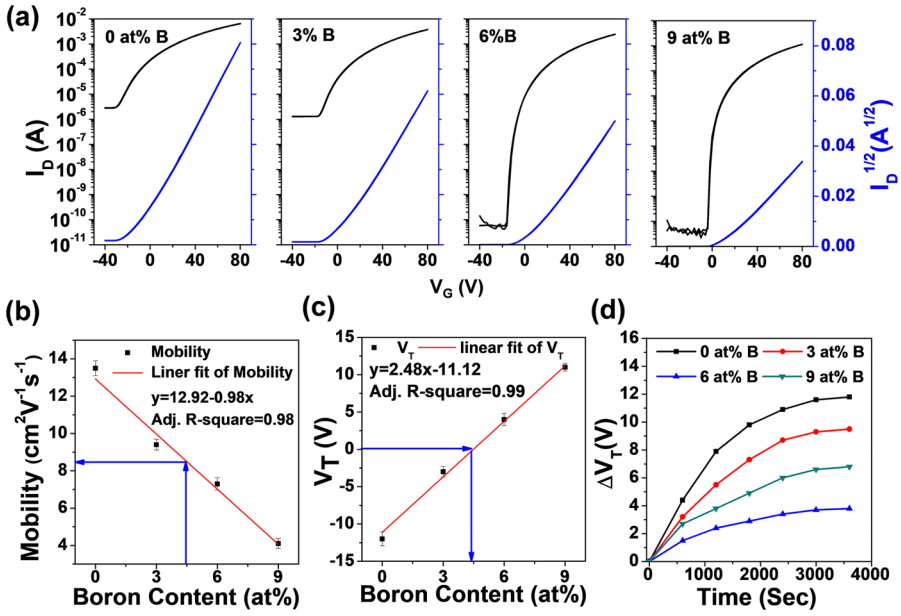

Figure 2. Charge transport of IBO films. (a) TFT transfer curves (at V_{DS} = 80 V). (b) Mobility−B atom % plot and linear interpolation. (c) V_T−B atom % plot and linear interpolation. The blue arrows are guides to the eyes to indicate composition affording near-zero V_T and the corresponding mobility. (d) Shifts in the threshold voltage of IBO TFTs with differing boron concentrations.

RESULTS AND DISCUSSION

Fabrication and Characterization of Boron-Doped In_2O_3 Films and Transistors. We first report the fabrication and characterization of IBO films and IBO TFTs with $n^{+2}Si/SiO_2$ gate contacts/dielectrics, to assess the role of B in modulating charge transport and to identify optimal compositions for TFT channels (Figure 1a). MO films are grown by spin-coating acetylacetone-based combustion solutions $[In(NO_3)_3{\cdot}xH_2O + H_3BO_3 + AcAcH + NH_4OH + 2$-methoxyethanol] on n^{+2}-Si/300 nm SiO_2 wafers. Boric acid is the B source for IBO films with B atomic % expressed as [B]/[In+B] = 3 atom % B, 6 atom % B, and 9 atom % B. The spin-coated films were annealed at 300 °C for 20 min, and this process is repeated four times. Finally, the devices were completed by thermally evaporating 40 nm thick Al source and drain electrodes.

To investigate how B incorporation affects IBO film microstructure, grazing incident X-ray diffraction (GIXRD, Figure 1b) and X-ray reflectivity (XRR, Figure 1c) measurements were carried out. Pristine In_2O_3 films processed at 300 °C are polycrystalline as evidenced by the strong (222) reflection at 2θ = 31.1° and weaker (211), (004) reflections at 2θ = 22.1° and 35.5°. Independent of B doping level, only broad peaks are observed for IBO films, indicating that B effectively frustrates In_2O_3 film crystallization. XRR data fitted with Igor-based MOTOFIT package[37] indicate that the IBO film thicknesses contract slightly with increasing B content, ranging from 8.9 nm (0 atom % B) to 8.5 nm (9 atom % B). The neat In_2O_3 films exhibit slight electron density fluctuations in the vertical direction with an average of 1.7 e $Å^{-3}$, while the 9 atom % B films are more uniform with a slightly lower average electron density of 1.6 e $Å^{-3}$. The surface morphologies of the IBO films were next assessed by AFM (Supporting Information Figure S1, Table S2) which reveals that all films are extremely smooth with RMS roughnesses between 0.19 and 0.21 nm.

X-ray photoelectron spectroscopy (XPS) was next performed to investigate the IBO film composition and oxygen bonding. Note that the XPS-derived atom % B content is in reasonable agreement with that of the precursor solutions (Supporting Information Figure S2a−c). The XPS oxygen peaks can be consistently deconvoluted into three individual subpeaks reflecting different O environments (Figure 1e). The dominant peak centered at 529.8 ± 0.1 eV arises from O atoms bonded to nearest-neighbor metal ions (M−O−M) in the lattice, the peak at 531.1 ± 0.1 eV is attributed to O atoms in the vicinity of an O vacancy, and the peak at highest binding energy, 532.2 ± 0.1 eV, can be assigned to surface O such as hydroxyls (M−OH).[38,39] To achieve superior electrical performance an MO semiconductor should maximize M−O−M formation/densification and minimize the detrimental O vacancies and M−OH densities.[40] Thus, an instructive method to correlate XPS results with fabricated TFT performance is to compare the ratio of the lowest binding energy O 1s subpeak M−O−M area to the total O 1s peak area, defined here as η_{M-O-M}. Figure 1f shows that η_{M-O-M} first increases from 73.4% to 79.5% as the B concentration increases from 0 to 6 atom %, then falls to 77.5% for excess B doping of 9 atom %. Note that this trend is consistent with the XPS results carried out on films without surface etching (Figure S2d); thus, the doping process does not affect the bulk chemical environment within these thin films. This result indicates that B acts as an effective O vacancy suppressor as a consequence of the strong B−O bonding. The subsequent decline in η_{M-O-M} with excess B may reflect incomplete dehydration of residual $B(OH)_3$. A similar study reported that Zr doping of ZnO films reduces O-related defect states.[41]

The transport characteristics of IBO TFTs using 300 nm SiO_2 (areal capacitance C_i = 11.5 nF cm^{-2}) as the gate dielectric and measured in ambient reveal that B doping has a profound influence on the TFT performance. Supporting Information Figure S3 shows IBO TFT output characteristics with clear pinch-off, linear, and saturated regions. From the transfer curves in Figure 2a, note that the pristine In_2O_3 TFTs

DOI: 10.1021/jacs.8b06395
J. Am. Chem. Soc. XXXX, XXX, XXX−XXX

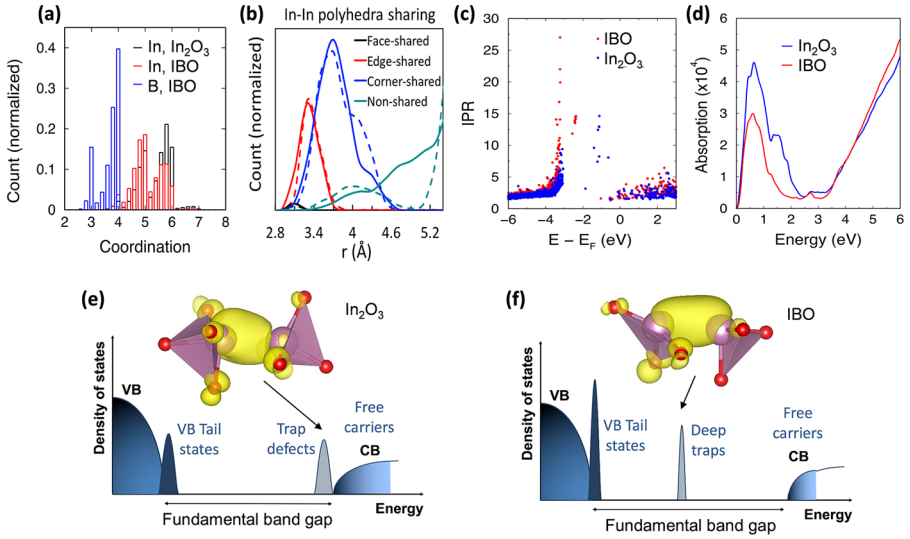

Figure 3. Calculated properties of amorphous In_2O_3 and IBO. (a) Distribution of In and B coordination as calculated via averaging over 5000-step MD simulations at 25 °C. ((b) InO polyhedra sharing as a function of the In−In distance for the oxide with (solid line) and without (dash line) boron. (c) Inverse participation ratio calculated for the valence, conduction, and gap states using the HSE approximation. (d) Optical absorption calculated using HSE approximation. Schematic of density of states and the calculated charge density for the electron trap defect state in (e) In_2O_3 and (f) IBO.

exhibit large off-state currents (~10^{-6} A), owing to the aforementioned excess carrier concentration. However, the I_{off} of IBO TFTs falls to ~10^{-11} A as the B atom % increases from 0% to 6%, and then stabilizes at a higher B content (9 atom %). Thus, the current on−off ratio of optimized IBO TFTs is 10^7, far greater than that (10^3) of In_2O_3 TFTs. For IBO $I-V$ characteristics, μ and threshold V_T were extracted using conventional MOSFET equations[10] and Table S2 reveals that μ decreases from 13.5 to 4.1 $cm^2\ V^{-1}\ s^{-1}$ and V_T shifts from −12 to +11 V as atom % B increases from 0 to 9 atom %, respectively, due to suppressed O vacancies. The subthreshold swing (SS) was also measured using the maximum slope in the transfer curve, and decreases substantially with increasing atom % B, from 14 V dec^{-1} for In_2O_3 TFTs to 0.6 V dec^{-1} for the 9 atom % IBO devices. Finally, Figure 2b and c plots mobility and V_T as a function of atom % B, respectively. Interestingly, both parameters exhibit an excellent linear correlation with the B concentration, achieving adjusted R-square values of 0.98 and 0.99, respectively. From these correlations, to achieve V_T ~ 0.0 V would require ~5 atom % B doping and yield μ ~ 8 $cm^2\ V^{-1}\ s^{-1}$. To test the reliability of this estimation, such a device was fabricated using identical processing conditions (see Experimental Section for details). The corresponding TFTs (representative data in Supporting Information Figure S4) exhibit a field effect mobility of 8.1 ± 0.31 $cm^2\ V^{-1}\ s^{-1}$ and a threshold voltage of 0 ± 0.43 V, fully consistent with the aforementioned linear models.

MO TFT performance erosion under bias stress is known to reflect charge trapping at the semiconductor-dielectric interface and in the dielectric layer.[42] The trapped electrons reduce the effective applied gate voltage, resulting in a positive V_T shift. It is reasonable that solution processed MO systems contain residual hydroxyl groups due to incomplete dehydration and condensation to a dense M−O−M framework. These can provide an additional source of localized states influencing bias stress response.[9] To investigate IBO TFT bias stress stability, these devices were subjected to a V_G-V_{DS} constant bias of +20 V for 600 s intervals for 3600 s in ambient, without intentional light blocking. The resulting TFT transfer plots shown in Figure S5 (Supporting Information) and bias stress induced V_T shifts with increasing bias time are plotted in Figure 2d. Although all IBO TFTs exhibit positive shifts upon bias, note that as B doping is increased from 0 to 6 atom %, there is a significant reduction in TFT V_T shift (ΔV_T) with ΔV_T decreasing from ~13.1 V (In_2O_3) to as low as ~3.5 V (6 at B%). However, as the B% doping approaches 9 atom %, bias stress stability begins to deteriorate. These results are in accord with the reduced O vacancies observed by XPS when B doping approaches 6 at B%.

Theoretical Calculations on Boron-Doped Indium Oxide Films. Ab initio MD simulations and DFT calculations next were performed to study the structure and electronic properties of IBO films. To achieve reliable statistics regarding the structural preferences of B and its effect on the electronic properties, 0 and 11 atom % B concentrations were used. First, the effective coordination number (ECN) was calculated for each metal atom at 25 °C over 5000 steps (10 ps). The ECN distributions for In−O and B−O are shown in Figure 3a. Due to the presence of B, the number of high-coordinated In atoms (ECN > 5.5) decreases, whereas the number of low-coordinated In atoms (ECN < 5.0) increases compared to In_2O_3. The average ECN of In−O is 5.0 for IBO, which is a notable reduction from ECN = 5.3 for In_2O_3. In IBO, the B atoms are primarily 4-coordinated with an average ECN of B−O of 3.6 and an average B−O distance of 1.47 Å, although nearly 20% of B atoms have trigonal coordination (with an average B−O distance of 1.38 Å) as found in B_2O_3 glass.[43] The calculated B−O distances and O−B−O angles in IBO closely match those in B_2O_3 suggesting that strong B−O bonding is maintained in IBO.

In addition to reducing In coordination, the presence of B affects the InO-InO polyhedra sharing, shown in Figure 3b. Boron favors short distance (below 3.1 Å) edge-shared In−In pairs and, at the same time, suppresses the number of corner-shared In−In polyhedra around 4.3 Å, that corresponds to the third In shell in crystalline In_2O_3.[33] Importantly, B reduces the

DOI: 10.1021/jacs.8b06395
J. Am. Chem. Soc. XXXX, XXX, XXX−XXX

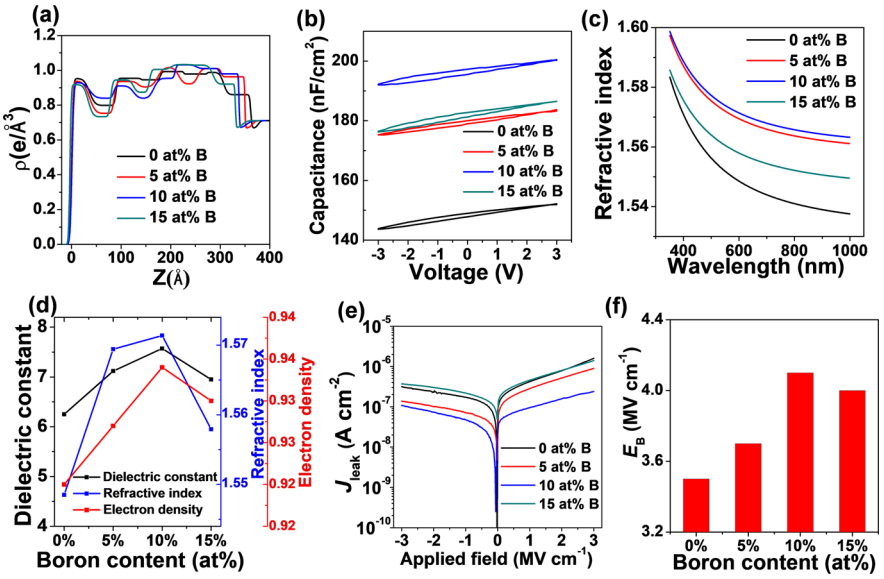

Figure 4. Properties of ABO dielectric films. (a) Electron density profiles. (b) Capacitance–voltage curves. (c) Refractive index–wavelength curves. (d) Plots of refractive index, dielectric constants, and average electron density as a function of B content. (e) Current density–voltage curves. (f) Breakdown field (E_B) of the ABO films with different B concentrations.

number of nonshared polyhedra with 3.4–4.2 Å In–In distances. The latter have been shown to be a source of defects in undoped In_2O_3.[44] Therefore, B addition is expected to suppress the number of structural defects responsible for carrier-generation and electron trapping in In_2O_3.

To better understand how B doping affects charge transport, DFT calculations were performed using the Scuseria–Ernzerhof (HSE) hybrid functional to accurately compute the electronic properties of the present amorphous wide-bandgap oxides. The inverse participation ratio (IPR) plots that illustrate the degree of localization of states near the band edges and within the gap are compared for amorphous indium oxide with and without B in Figure 3c. First of all, the IPR results reveal that the IBO states at and above the Fermi level are more localized than in the B-free structure (Figure 3c) meaning that the conduction paths become "narrower" upon B doping since the B 2s states are significantly higher in energy than the In 5s states and, hence, unavailable to free electrons. Furthermore, the reduced number of octahedrally coordinated InO_6 polyhedra in IBO (Figure 3a) indicates that InO_6 chain formation which facilitates electron conduction in amorphous In_2O_3 is hindered by the presence of B.[33,44] All the above data, along with a stronger electron scattering at the localized defects (vide infra), explain the observed decline in electron mobility with increasing B content (Figure 2a).

To study the role of B in the formation of electron trap defects, MD liquid-quench simulations were performed for O-substoichiometric oxides. In undoped $In_2O_{2.92}$ (corresponding to an O/M ratio = 1.46), the defect states appear at about 1.2 eV below the Fermi level and spread over a wide energy range, ΔE, of 0.8 eV. At the same O substoichiometry in B:$In_2O_{2.92}$, the defect states are deeper, located at about 2.6 eV below the Fermi level, have a narrow ΔE = 0.2 eV energy range, and are strongly localized as indicated by the high IPR value in Figure 3c. For comparison, the defect states in Ga:$In_2O_{2.92}$ at the same doping concentration (11 atom % Ga) are less localized, appearing at 2.1 eV below the Fermi level with a 0.4 eV energy range. This is consistent with stronger deviations in the Ga–O distances and O–Ga–O angles in amorphous IGO from those in crystalline Ga_2O_3.[45] Thus, the degree of localization and energetic location of the electron trap defects with respect to the conduction band edge of the host oxide increases with the bond strength of the dopant.

The calculated charge density distribution for the defect states in $In_2O_{2.92}$ and B:$In_2O_{2.92}$, shown in Figure 3e and f, reveals the origin of the different degree of localization: in both cases, the electron density is localized between two under-coordinated In atoms located ca. 2.7 Å from each other; however, in $In_2O_{2.92}$ the coordination numbers of the two In atoms are 3.80 and 3.86, whereas in B:$In_2O_{2.92}$ the In coordination numbers are far lower, 2.60 and 2.75. Furthermore, since the number of nonshared In pairs decreases in the presence of B (Figure 3b), the defect is more localized than the one in the B-free oxide where a larger fraction of nonshared In–In pairs in the cell ensures the existence of states with compatible energy, i.e., available for the trapped electron. Therefore, the lower coordination of In atoms associated with the presence of B (Figure 3a) combined with the lack of nonshared In pairs with comparable energies (Figure 3b), favors the formation of deep, strongly localized defects, as illustrated in the schematic density of states shown in Figure 3e and f.

The calculated IBO optical properties in Figure 3d show that B doping helps maintain low absorption across the entire visible range. Although B increases the fundamental In_2O_3 band gap (that of B_2O_3 glass is computed to be 8 eV), the optical band gaps of In_2O_3 and IBO are identical (3.1 eV, Figure 3d), implying a smaller Burstein–Moss shift in IBO owing to a smaller free electron density in this material as signified by lower infrared absorption versus that in In_2O_3. Simultaneously, the strong localization of the deep trap defects in IBO results in a small absorption within the visible range—in contrast to undoped In_2O_3 where the defect causes significant absorption at 1.4–2.2 eV (Figure 3d).

Finally, we analyze transistor stability from a theoretical standpoint. The following factors contribute to instability under applied voltage in undoped In_2O_3 TFTs: (1) Close energy proximity of the trap defects to the conduction band;

DOI: 10.1021/jacs.8b06395
J. Am. Chem. Soc. XXXX, XXX, XXX–XXX

(2) wide energy range of the defect states; and (3) relatively weak localization of the defects. Due to all the above phenomena, trapped electrons can easily escape into the conduction band under a bias causing the threshold voltage shift discussed above. The addition of small B concentrations reduces the number of carriers and leads to deeper and more localized trap defects, thereby reducing the probability for trapped electrons to escape. Hence, the material with small B content shows better stability. At higher B concentrations, however, the device stability deteriorates due to coordination transformations of B. Boron is primarily four-coordinate at low doping concentration, but the fraction of trigonal boron atoms increases with the B concentration (in B_2O_3 glass all B atoms have trigonal coordination). The B coordination evolution from 4- to 3-coordinated, shown in Supporting Information Figure S6d, results in weakly bound O atoms in the amorphous state. Diffusion of such O atoms may compensate the deep defects associated with under-coordinated under-shared In atoms, leading to enhanced instability under bias stress conditions as observed experimentally.

Growth, Characterization, and Modeling of Boron-Doped Aluminum Oxide Dielectrics. To expand the scope of this study, we explored the effects of also B-doping of a TFT dielectric material fabricated by solution spin-coating/combustion synthesis. B-doped Al_2O_3 (ABO) precursor solutions were prepared using $Al(NO_3)_3$, H_3BO_3, and 2-methoxyethanol as the solvent in an acetylacetone-based combustion process. The ABO films, having 5, 10, and 15 atom % B content vs B+Al, were deposited by spin-coating on n^{+2}-Si wafers and then annealed at 300 °C for 20 min. After repeating the above process four times, the films were postannealed at 450 °C for 1 h in air.

GIXRD and AFM (Supporting Information Figures S7 and S8a) show that all the ABO films are amorphous and have very smooth surfaces ($\sigma_{RMS} \sim 0.1$ nm). XRR (Figures 4a and S8b) indicates that the ABO film thickness falls slightly from 36.2 to 33.2 nm with increasing B content (Supporting Information Table S3). Next, to assess film electrical quality, metal−insulator−semiconductor (MIS) capacitors were fabricated with Al top electrodes. Capacitance−voltage ($C-V$, Figure 4b) and capacitance−frequency ($C-f$, Supporting Information Figure S8c) measurements in ambient reveal a small hysteresis window, indicating negligible mobile ions or trapped charges in the films.[46] The calculated relative dielectric constants for the 0, 5, 10, and 15 atom % ABO films are 6.25, 7.12, 7.57, and 6.95, respectively (Figure 4d). Values for the undoped films are similar to other solution-processed Al_2O_3 films.[47−49]

Figure 4c shows ABO film refractive index-wavelength plots. Note that as the B doping increases from 0 to 10 atom % the refractive index at 600 nm increases from 1.548 to 1.571. When the atom % B concentration reaches 15 atom %, the refractive index then falls to 1.558. These values are somewhat higher than those reported by Vitanov for Al_2O_3 thin films grown by the sol−gel technique.[50] The plots of Figure 4d indicate that the variations of ABO film dielectric constant, refractive index, and average electron density are correlated, and indicate that higher refractive index tracks enhanced dielectric properties. ABO film electrical and optical data as a function of atom % B are summarized in Supporting Information Table S3.

MD simulations and DFT calculations on amorphous Al_2O_3 and ABO (11 atom % B) were next carried out to understand the experimental optical properties. Specifically, theory reveals that, similar to IBO, B maintains the strong bonding with O atoms in ABO, evidenced by the average B−O distances of 1.35−1.38 Å and 1.46−1.48 Å for trigonal and tetrahedral B coordination, respectively. The presence of B suppresses the number of octahedrally coordinated Al atoms and increases the number of 4-coordinated Al (Supporting Information Figure S9a). Accordingly, the number of edge-shared (corner-shared) Al−Al pairs decreases (increases) as the B content increases (Supporting Information Figure S9b). As a result, the calculated refractive index increases from 1.37 for amorphous bulk Al_2O_3 to 1.38 for Al_2O_3 with 11 atom % B substitution, in accord with the experimental trends (Supporting Information Table S3). The role of corner-shared 4-coordinated Al atoms in enhancing the refractive index can be derived by comparing the optical properties of crystalline alumina phases: in α-Al_2O_3 with 6-coordinated Al, the calculated refractive index is 1.40, whereas in θ-Al_2O_3 with half of the Al atoms having 4-fold coordination it increases to 1.48. Higher B concentrations in amorphous Al_2O_3 (in these calculations, 11 and 19 atom % B were studied) does not affect the Al coordination distribution or Al−Al sharing (Supporting Information Figure S9a); however, B coordination undergoes a transformation from tetrahedral to a mix of tetrahedral and trigonal. Because the calculated refractive index of amorphous B_2O_3 with trigonal B atoms ($n = 1.22$) is lower than that of amorphous Al_2O_3 ($n = 1.37$), the presence of a large fraction of trigonal B in ABO (Supporting Information Figure S9a) explains the lower refractive index at 15 atom % boron.

Figure 4e shows the current density−voltage ($J-V$) characteristics of the present ABO films. All the current density values vary exponentially with the voltage, in accord with Poole−Frenkel (PF) conduction and Schottky emission mechanisms, two of the most common models describing thin film conduction.[51] J at 3 MV cm^{-1} first decreases from 1.6×10^{-6} to 2.3×10^{-7} A cm^{-2} as the atom % B increases from 0 to 10% and then increases to 1.4×10^{-6} A cm^{-2} for the largest 15%. Furthermore, according to Figure 4f, the 10 atom % B doped film also exhibits a higher breakdown field of 4.1 MV cm^{-1}. This result likely reflects the large B−O bond dissociation energy discussed above which effectively suppresses O vacancy formation. Generally, O vacancies in high-k dielectric materials have been related to space-charge formation which creates deep-trap energy levels in the band gap for activated electrons to be mobile. So the more O vacancies, the more free carriers can be generated.[52] When the ABO atom % B first increases, high densities of M−O−M units are formed, enhancing the dielectric strength. However, when the B concentration increases further to 15 atom %, the leakage current increases and the breakdown field falls. This may reflect defect formation by excess impurities (vide supra) as reported for B-doped Zr oxide dielectrics.[11]

TFTs Based on Boron-Doped MO Channel and Dielectric Layers. To demonstrate the attraction of ABO films as gate dielectrics and their integratibility with IBO semiconductors, bottom-gate 6 atom % IBO/10 atom % ABO TFTs were fabricated on n^{+2}-Si wafers with top-contact Al source/drain electrodes. These IBO and ABO compositions were selected on the basis of the optimized properties discussed above. Note that devices having 6 atom % IBO with Al_2O_3 were also fabricated and their electrical characteristics assessed for comparison. Cross-sectional TEM and STEM were performed on 6 atom % IBO/10 atom % ABO bilayers to investigate the microstructural characteristics.

DOI: 10.1021/jacs.8b06395
J. Am. Chem. Soc. XXXX, XXX, XXX−XXX

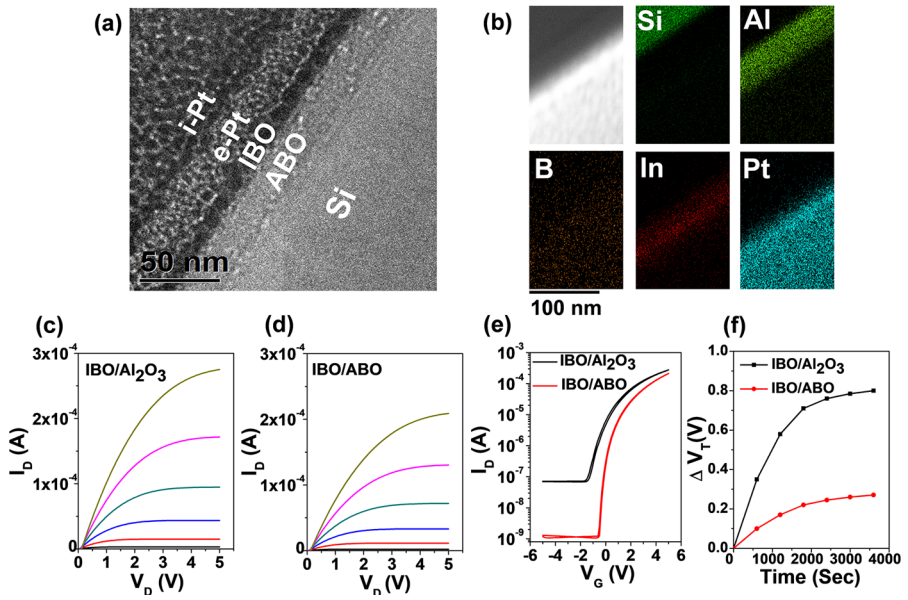

Figure 5. Morphology and charge transport of IBO-ABO films (a) Cross-sectional TEM images of the IBO-ABO bilayer. (b) STEM and energy-dispersive X-ray spectroscopy scans of Si, In, B, Al, and Pt. (c) Output curves of the IBO/Al_2O_3 TFT (V_G = 0−5 V, 1 V interval). (d) Output curves of the IBO/ABO TFT (V_G = 0−5 V, 1 V interval). (e) Transfer curves of both type of TFTs (at V_{DS} = 5 V). (f) Bias stress stability of the indicated TFTs.

Figure 5a shows the well-defined layers with uniform thicknesses across the film samples. The high-quality contacts between the gate electrode and dielectric layer, dielectric layer, and semiconductor layer should ensure good gate modulation, low densities of electron trap sites, and low contact resistance. The colored elemental mapping images and energy-dispersive X-ray spectroscopy (EDX) line-scan profiles of the element distributions shown in Figures 5b and S10 indicate formation of continuous multilayer structures with negligible inter-penetration. To further confirm the presence and assess the boron content in ABO films, XPS was performed for the 10 atom % B ABO sample. The Al 2p, B 1s, and O 1s XPS peaks shown in Figure S11 reveal that the B/[B + Al] is 10.8% B, thus very close to the nominal synthetic concentration.

As shown in Figure 5c−e, TFTs with 10 atom % ABO and Al_2O_3 dielectrics exhibit excellent output and transfer curves. According to the thicknesses and dielectric constants measured above, the areal capacitances (C_i) of Al_2O_3 and 10 atom % ABO dielectric are 149 and 196 nF cm^{-2}, respectively (Supporting Information Table S4). For 6 atom % IBO/Al_2O_3 TFTs, the mobility, current on/off ratio, threshold voltage, and subthreshold slope are 9.7 cm^2 V^{-1} s^{-1}, 10^4, −0.9, and 0.79 V dec^{-1}, respectively. In contrast, the 6 atom % IBO TFTs with a 10 atom % B ABO dielectric have a higher mobility of 11.3 cm^2 V^{-1} s^{-1}, a threshold voltage of 0.6 V, a larger current on/off ratio of 2 × 10^5, and a smaller subthreshold slope of 0.17 V. Finally, to evaluate the electrical stability of these devices, positive gate bias stress experiments using V_G = +3 V for 3600 s were carried out (Supporting Information Figure S12). A ΔV_T of only +0.25 V is measured for the ABO device (Figure 5f), significantly smaller than that using Al_2O_3 (ΔV_T = +0.8 V), demonstrating the superior stability properties of the B-doped MO pair.

CONCLUSION

In summary, an effective approach is reported to enhance the performance of metal oxide TFTs by boron doping *both* the channel and dielectric layers, and the mechanism analyzed by experiment and theory. It is found that the appropriate boron doping in the In_2O_3 TFT channel frustrates crystallization and acts as a carrier suppressor. For the adjacent Al_2O_3 dielectric film, optimal boron doping enhances the refractive index and dielectric constant, and reduces the leakage current density. TFTs having both B-doped channel and dielectric layers were fabricated by solution processing, and exhibit excellent performance, with a field effect mobility of 11.3 cm^2 V^{-1} s^{-1}, a threshold voltage of 0.6 V, a current on/off current ratio of 2 × 10^5, and a subthreshold swing of 0.17 V dec^{-1} with excellent bias-stress stability. A generalizable atomistic model of how small, Lewis acidic dopants such as B operate is developed based on combined theoretical and experimental results.

ASSOCIATED CONTENT

Supporting Information

The Supporting Information is available free of charge on the ACS Publications website at DOI: 10.1021/jacs.8b06395.

GIXRD and XPS data, AFM and TEM images of thin films, transfer and output curves, bias-stress test and electrical parameters of TFTs, and theoretical calculation of IBO and ABO (PDF)

AUTHOR INFORMATION

Corresponding Authors

*t-marks@northwestern.edu
*a-facchetti@northwestern.edu
*juliaem@mst.edu
*wfzhang@henu.edu.cn

ORCID

Binghao Wang: 0000-0002-9631-6901
Wei Huang: 0000-0002-0973-8015
Yao Chen: 0000-0003-4414-8528
Li Zeng: 0000-0001-6390-0370
Weigang Zhu: 0000-0002-5888-4481

DOI: 10.1021/jacs.8b06395
J. Am. Chem. Soc. XXXX, XXX, XXX−XXX

Michael J. Bedzyk: 0000-0002-1026-4558
Antonio Facchetti: 0000-0002-8175-7958
Tobin J. Marks: 0000-0001-8771-0141

Author Contributions

[⊥]X. Z. and B.W. contributed equally.

Notes

The authors declare no competing financial interest.

■ ACKNOWLEDGMENTS

We thank US-Israel Binational Science Foundation (BSF) (AGMT-2012250///02), ONR (MURI N00014-11-1-0690), the Northwestern U. MRSEC (NSF DMR-1720139), and Flexterra Corp. for support of this research. A. F. thanks the Shenzhen Peacock Plan project KQTD20140630110339343 for support. J.E.M. thanks the NSF-DMREF program (DMR-1729779) and XSEDE (DMR-080007) for support. X.Z. thanks the China Scholarship Council for support, the National Natural Science Foundation of China (Grant No. U1504625) and the youth backbone teacher training program in He'nan province (Grant No. 2017GGJS021). This work made use of the J. B. Cohen X-ray Diffraction Facility, EPIC facility, Keck-II facility, and SPID facility of the NUANCE Center at Northwestern U., which received support from the Soft and Hybrid Nanotechnology Experimental (SHyNE) Resource (NSF NNCI-1542205); the MRSEC program (NSF DMR-1720139) at the Materials Research Center; the International Institute for Nanotechnology (IIN); the Keck Foundation; and the State of Illinois, through the IIN.

■ REFERENCES

(1) Yu, X.; Marks, T. J.; Facchetti, A. *Nat. Mater.* **2016**, *15* (4), 383−96.
(2) Koida, T.; Kondo, M. *J. Appl. Phys.* **2007**, *101* (6), 063705.
(3) Buchholz, D. B.; Liu, J.; Marks, T. J.; Zhang, M.; Chang, R. P. *ACS Appl. Mater. Interfaces* **2009**, *1* (10), 2147−53.
(4) Seo, J. S.; Jeon, J. H.; Hwang, Y. H.; Park, H.; Ryu, M.; Park, S. H.; Bae, B. S. *Sci. Rep.* **2013**, *3*, 2085.
(5) Zhang, F.; Liu, G.; Liu, A.; Shin, B.; Shan, F. *Ceram. Int.* **2015**, *41* (10), 13218−13223.
(6) Jeong, S.; Ha, Y.-G.; Moon, J.; Facchetti, A.; Marks, T. J. *Adv. Mater.* **2010**, *22* (12), 1346−1350.
(7) Aikawa, S.; Nabatame, T.; Tsukagoshi, K. *Appl. Phys. Lett.* **2013**, *103* (17), 172105.
(8) Mitoma, N.; Aikawa, S.; Ou-Yang, W.; Gao, X.; Kizu, T.; Lin, M.-F.; Fujiwara, A.; Nabatame, T.; Tsukagoshi, K. *Appl. Phys. Lett.* **2015**, *106* (4), 042106.
(9) Kim, H. J.; Je, S. Y.; Won, J. Y.; Baek, J. H.; Jeong, J. K. *Phys. Status Solidi RRL* **2014**, *8* (11), 924−927.
(10) Huang, W.; Zeng, L.; Yu, X.; Guo, P.; Wang, B.; Ma, Q.; Chang, R. P. H.; Yu, J.; Bedzyk, M. J.; Marks, T. J.; Facchetti, A. *Adv. Funct. Mater.* **2016**, *26* (34), 6179−6187.
(11) Park, J. H.; Yoo, Y. B.; Lee, K. H.; Jang, W. S.; Oh, J. Y.; Chae, S. S.; Lee, H. W.; Han, S. W.; Baik, H. K. *ACS Appl. Mater. Interfaces* **2013**, *5* (16), 8067−8075.
(12) Secor, E. B.; Smith, J.; Marks, T. J.; Hersam, M. C. *ACS Appl. Mater. Interfaces* **2016**, *8* (27), 17428−34.
(13) Manoharan, C.; Jothibas, M.; Jeyakumar, S. J.; Dhanapandian, S. *Spectrochim. Acta, Part A* **2015**, *145*, 47−53.
(14) Gandla, S.; Gollu, S. R.; Sharma, R.; Sarangi, V.; Gupta, D. *Appl. Phys. Lett.* **2015**, *107* (15), 152102.
(15) Aikawa, S.; Mitoma, N.; Kizu, T.; Nabatame, T.; Tsukagoshi, K. *Appl. Phys. Lett.* **2015**, *106* (19), 192103.
(16) Parthiban, S.; Kwon, J.-Y. *J. Mater. Res.* **2014**, *29* (15), 1585−1596.
(17) Smith, J.; Zeng, L.; Khanal, R.; Stallings, K.; Facchetti, A.; Medvedeva, J. E.; Bedzyk, M. J.; Marks, T. J. *Adv. Electron. Mater.* **2015**, *1* (7), 1500146.
(18) Parthiban, S.; Kwon, J.-Y. *J. Mater. Chem. C* **2015**, *3* (8), 1661−1665.
(19) Stewart, K. A.; Gouliouk, V.; Keszler, D. A.; Wager, J. F. *Solid-State Electron.* **2017**, *137*, 80−84.
(20) Jo, J. W.; Kim, J.; Kim, K. T.; Kang, J. G.; Kim, M. G.; Kim, K. H.; Ko, H.; Kim, Y. H.; Park, S. K. *Adv. Mater.* **2015**, *27* (7), 1182−8.
(21) Yang, J.; Liao, P.-Y.; Chang, T.-C.; Chen, B.-W.; Huang, H.-C.; Su, W.-C.; Chiang, H.-C.; Zhang, Q. *Appl. Phys. Lett.* **2017**, *110* (14), 143508.
(22) Wang, B.; Zeng, L.; Huang, W.; Melkonyan, F. S.; Sheets, W. C.; Chi, L.; Bedzyk, M. J.; Marks, T. J.; Facchetti, A. *J. Am. Chem. Soc.* **2016**, *138* (22), 7067−74.
(23) Kim, M. G.; Kanatzidis, M. G.; Facchetti, A.; Marks, T. J. *Nat. Mater.* **2011**, *10* (5), 382−8.
(24) Yu, X.; Smith, J.; Zhou, N.; Zeng, L.; Guo, P.; Xia, Y.; Alvarez, A.; Aghion, S.; Lin, H.; Yu, J.; Chang, R. P.; Bedzyk, M. J.; Ferragut, R.; Marks, T. J.; Facchetti, A. *Proc. Natl. Acad. Sci. U. S. A.* **2015**, *112* (11), 3217−22.
(25) Kresse, G.; Hafner, J. *Phys. Rev. B: Condens. Matter Mater. Phys.* **1993**, *47* (1), 558−561.
(26) Kresse, G.; Hafner, J. *Phys. Rev. B: Condens. Matter Mater. Phys.* **1994**, *49* (20), 14251−14269.
(27) Kresse, G.; Furthmuller, J. *Comput. Mater. Sci.* **1996**, *6*, 15.
(28) Kresse, G.; Furthmuller, J. *Phys. Rev. B: Condens. Matter Mater. Phys.* **1996**, *54*, 11169.
(29) Perdew, J. P.; Burke, K.; Ernzerhof, M. *Phys. Rev. Lett.* **1996**, *77* (96), 3865.
(30) Blöchl, P. E. *Phys. Rev. B: Condens. Matter Mater. Phys.* **1994**, *50* (24), 17953−17979.
(31) Kresse, G.; Joubert, D. *Phys. Rev. B: Condens. Matter Mater. Phys.* **1999**, *59* (99), 1758.
(32) Hoppe, R. *Angew. Chem., Int. Ed. Engl.* **1970**, *9* (1), 25−34.
(33) Buchholz, D. B.; Ma, Q.; Alducin, D.; Ponce, A.; Jose-Yacaman, M.; Khanal, R.; Medvedeva, J. E.; Chang, R. P. *Chem. Mater.* **2014**, *26* (18), 5401−5411.
(34) Heyd, J.; Scuseria, G. E.; Ernzerhof, M. *J. Chem. Phys.* **2003**, *118* (18), 8207−8215.
(35) Heyd, J.; Peralta, J. E.; Scuseria, G. E.; Martin, R. L. *J. Chem. Phys.* **2005**, *123* (17), 174101.
(36) Momma, K.; Izumi, F. *J. Appl. Crystallogr.* **2011**, *44* (6), 1272−1276.
(37) Nelson, A. *J. Appl. Crystallogr.* **2006**, *39* (2), 273−276.
(38) Hennek, J. W.; Smith, J.; Yan, A.; Kim, M. G.; Zhao, W.; Dravid, V. P.; Facchetti, A.; Marks, T. J. *J. Am. Chem. Soc.* **2013**, *135* (29), 10729−41.
(39) Ji, K. H.; Kim, J.-I.; Jung, H. Y.; Park, S. Y.; Choi, R.; Kim, U. K.; Hwang, C. S.; Lee, D.; Hwang, H.; Jeong, J. K. *Appl. Phys. Lett.* **2011**, *98* (10), 103509.
(40) Lee, S.-H.; Kim, T.; Lee, J.; Avis, C.; Jang, J. *Appl. Phys. Lett.* **2017**, *110* (12), 122102.
(41) Park, J.-S.; Kim, K.; Park, Y.-G.; Mo, Y.-G.; Kim, H. D.; Jeong, J. K. *Adv. Mater.* **2009**, *21* (3), 329−333.
(42) Yang, J.; Pi, S.; Han, Y.; Fu, R.; Meng, T.; Zhang, Q. *IEEE Trans. Electron Devices* **2016**, *63* (5), 1904−1909.
(43) Xu, Q.; Kawamura, K.; Yokokawa, T. *J. Non-Cryst. Solids* **1988**, *104*, 261−272.
(44) Medvedeva, J. E.; Buchholz, D. B.; Chang, R. P. H. *Adv. Electron. Mater.* **2017**, *3* (9), 1700082.
(45) Moffitt, S. L.; Zhu, Q.; Ma, Q.; Falduto, A. F.; Buchholz, D. B.; Chang, R. P. H.; Mason, T. O.; Medvedeva, J. E.; Marks, T. J.; Bedzyk, M. J. *Adv. Electron. Mater.* **2017**, *3* (10), 1700189.
(46) Zhang, S.; Kuo, Y.; Verkhoturov, S. *ECS Trans.* **2015**, *69*, 17−22.
(47) Furuta, M.; Kawaharamura, T.; Depang, W.; Toda, T.; Hirao, T. *IEEE Electron Device Lett.* **2012**, *33* (6), 851−853.

DOI: 10.1021/jacs.8b06395
J. Am. Chem. Soc. XXXX, XXX, XXX−XXX

(48) Kim, Y. G.; Avis, C.; Jang, J. *ECS Solid State Lett.* **2012**, *1* (2), Q23−Q25.
(49) Yang, W.; Song, K.; Jung, Y.; Jeong, S.; Moon, J. *J. Mater. Chem. C* **2013**, *1* (27), 4275−4282.
(50) Vitanov, P.; Harizanova, A.; Ivanova, T.; Dimitrova, T. *Thin Solid Films* **2009**, *517* (23), 6327−6330.
(51) Yu, S.; Li, L.; Zhang, W.; Xu, D.; Dong, H.; Jin, Y. *Mater. Chem. Phys.* **2014**, *148* (1−2), 426−430.
(52) Gao, R. L.; Yang, H. W.; Chen, Y. S.; Sun, J. R.; Zhao, Y. G.; Shen, B. G. *J. Alloys Compd.* **2014**, *591*, 346−350.

DOI: 10.1021/jacs.8b06395
J. Am. Chem. Soc. XXXX, XXX, XXX−XXX